Simulating horizontal crustal motions of glacial isostatic adjustment using compressible cartesian models

Reusen, J.M.; Steffen, R; Steffen, Holger; Root, B.C.; van der Wal, W.

DOI
10.1093/gji/ggad232

Publication date
2023

Document Version
Accepted author manuscript

Published in
Geophysical Journal International

Citation (APA)
Reusen, J. M., Steffen, R., Steffen, H., Root, B. C., & van der Wal, W. (2023). Simulating horizontal crustal motions of glacial isostatic adjustment using compressible cartesian models. *Geophysical Journal International*, *235*(1), 542-553. https://doi.org/10.1093/gji/ggad232

submitted to *Geophys. J. Int.*

Simulating horizontal crustal motions of glacial isostatic adjustment using compressible cartesian models

J. M. Reusen,[1] R. Steffen,[2] H. Steffen,[2] B. C. Root,[1] W. van der Wal[1]

[1] *Faculty of Aerospace Engineering, Delft University of Technology, Delft, The Netherlands*

[2] *Lantmäteriet, Gävle, Sweden*

Last compiled: 5 June 2023

SUMMARY

Significant land uplift and horizontal motions have been recorded with Global Navigation Satellite Systems (GNSS) in areas such as Alaska, Iceland, and the Northern Antarctic Peninsula (NAP) as a result of Glacial Isostatic Adjustment (GIA) due to ice melt after the Little Ice Age. Here, analysis of horizontal displacement rates can be of extra importance, as they are more sensitive to Earth properties in shallower layers than vertical displacement rates. Proper modelling of horizontal displacement rates with dedicated GIA models requires a spherical Earth with compressible rheology. However, in these small areas, the employed GIA models are often incompressible using a cartesian geometry to ease computation and in some cases allow for lateral viscosity changes or more complex rheology. We investigate the validity of modelled horizontal displacement rates using different approximations, i.e. using spherical or cartesian Earth structures, and incompressible, material compressible or compressible rheology. While the lack of self-gravity and sphericity compensate each other in the vertical, this is less the case for the horizontal. For a disc ice sheet with a radius just over 200 km and a thickness of 1,000 m, differences due to sphericity are minimal, and the modelled horizontal displacement rates of compressible cartesian models differ from those simulated by a compressible spherical model by 0.63 mm/a. Thus, compressible cartesian GIA models can be applied for modelling horizontal displacement rates of small ice sheets like those in Alaska, Iceland, and NAP. Unfortunately, the implementation of compressibility in Abaqus that we use here cannot be extended to spherical models as gravity can not be specified for a spherical body. Other modelling approaches are recommended in such cases.

Key words: Finite element method, Glaciology, Loading of the Earth, Mechanics, theory, and modelling

1 INTRODUCTION

In understanding Glacial Isostatic Adjustment (GIA) the observed horizontal motions of the crust generally receive less attention than the vertical motions, even though these horizontal motions are found to be very sensitive to lateral and radial variations in viscosity (e.g., Gasperini et al. 1990; O'Keefe & Wu 2002; Kaufmann et al. 2005; Latychev et al. 2005; Steffen et al. 2006; Hermans et al. 2018; Vardić et al. 2022). In addition, horizontal motions are significantly affected by compressibility (James & Lambert 1993; Mitrovica et al. 1994; Johnston et al. 1997; Tanaka et al. 2011), which is not supported by several commonly used GIA models.

In particular, GIA models which neglect sphericity generally do not include compressibility. To our knowledge, the only exceptions are Wolf et al. (1985), which is based on a uniform Earth model, and Klemann et al. (2003) which is no longer in use (Klemann, personal communication). Such 'cartesian models', as we will call them in the following, have been used for several applications. However, cartesian models either assume incompressibility (e.g., Ivins & James 1999; Larsen et al. 2003, 2004; Pagli et al. 2007; Schotman et al. 2008; Árnadóttir et al. 2009; Zwinger et al. 2020), or use material compressibility only (e.g., Kaufmann et al. 2005; Steffen et al. 2006; Lund et al. 2009; Auriac et al. 2013; Nield et al. 2018; Marsman et al. 2021). The latter refers to models in which the material is compressible, i.e. it has a Poisson ratio below 0.5, but the buoyancy forces are not adjusted for the change in density due to compressibility (Klemann et al. 2003). However, it is currently unclear how accurate the approximation of material compressibility is compared to full compressibility, where the internal buoyancy force is included in the equation of motion. Compressibility can also be approximated by adjusting the flexural rigidity, which is most accurate for smaller wavelength signals (Tanaka et al. 2011). Cartesian models are attractive because they provide a means to incorporate high spatial resolution and 3D variations in Earth structure with small computation times. In the following we will refer to models that can deal with 3D variations in Earth model parameters as 3D models.

Cartesian GIA models provide sufficient accuracy for the vertical deformation for ice sheets up to the size of the Fennoscandian ice sheet (Amelung & Wolf 1994; Wu & Johnston 1998), but for horizontal deformation this has been less thoroughly investigated. In this study, we will explore to what extent cartesian models can be used for GIA studies, for incompressible, material compressible, and fully compressible models. We thereby test a recently highlighted implementation of compressibility, and investigate possibilities to extend this to a spherical geometry.

We aim to answer the following research questions:

(1) How can we implement full compressibility in cartesian GIA models of Abaqus?

(2) How well are horizontal motions approximated by a cartesian model with (i) incompressibility, (ii) material compressibility and (iii) full compressibility as compared to a fully compressible spherical model?

We focus on the horizontal motions, as the effect of compressibility on the horizontal is larger, and the observations are to date relatively underused. To answer the first research question, we implement compressibility using the method of Hampel et al. (2019) for cartesian multi-layer models in Abaqus. We also briefly examine the method of Hampel et al. (2019) for spherical GIA models, but conclude that the method cannot be implemented in spherical models. We compare the cartesian model with a spherical compressible 1D model based on a semi-analytical method, and we include a case study of glacial unloading on top of a low-viscous mantle representative of the mantle in West Antarctica, Alaska, and Iceland. This provides recommendations for what applications the cartesian model, compressible or incompressible, can be used regarding analysis of horizontal motions and their observation.

2 THEORY

The software Abaqus is based on the finite element (FE) method. Two different implementations are described, which have been used in the modelling of the loading scenarios: (1) a model employing Elastic Foundations (EF, Wu 2004), similar to the model in Schotman et al. (2008), and (2) a "Non-linear geometry with explicit Gravity" (NG) model, described in Hampel et al. (2019). The EF model is employed in many GIA studies (e.g., Li et al. 2020; Lund et al. 2009; Nield et al. 2022; Steffen et al. 2006; van der Wal et al. 2015), and has been benchmarked for incompressible material parameters in Spada et al. (2011). It is used to validate the NG model implementation for the incompressible case. We start with a description of the governing equations of GIA, and how this is handled by the EF model. Afterwards, we introduce how the finite element equations are solved in Abaqus to better understand what is done in the NG model, and its differences with the EF model.

The conservation of momentum equation for external loading of a compressible Earth linearized with respect to hydrostatic equilibrium is given by (Wu & Peltier 1982):

$$\nabla \cdot \boldsymbol{\tau} - \nabla \left(\mathbf{u} \cdot \rho_0 g_0 \hat{r} \right) - \rho' g_0 \hat{r} - \rho_0 \nabla \phi' = 0. \tag{1}$$

Here, $\boldsymbol{\tau}$ is the Cauchy stress matrix, $\mathbf{u}$ is the displacement vector, ρ_0 and g_0 are the hydrostatic background density and gravity, respectively, $\hat{r}$ is the unit vector in the radial direction, ρ' denotes the density perturbation with respect to the hydrostatic background state, and ϕ' is the perturbation in the gravitational potential. Equation 1 contains four terms. The first term is the divergence of stress. The second term is the restoring force of isostasy (Wu 2004), which is an upwards force preventing the ice load from sinking indefinitely. The third term is the internal buoyancy force, caused by the change in the density of the individual elements due to dilatation. The density perturbation that is added to equation 1 is derived from the mass conservation equation (Backus 1967):

$$\rho' = -\nabla \cdot \left(\rho_0 \mathbf{u} \right). \tag{2}$$

For incompressible models, changes in density are zero (i.e. $\rho' = 0$) and the third term in equation 1 disappears. The fourth term in equation 1 represents the self-gravity. We will neglect the self-gravity in the cartesian models as this is not typically included in earlier studies with such models, partly because it is found to compensate the lack of sphericity (Amelung & Wolf 1994). However, it is present in the spherical NMM model that we use for validation, so we need to quantify that effect. In compressible models, the gravitational potential responds to a change in the density of the elements. The perturbed potential can be derived from Poisson's equation (Wu & Peltier 1982):

$$\nabla^2 \phi' = 4\pi G \rho'. \tag{3}$$

Here G is the gravitational constant. The corresponding boundary conditions for the GIA problem are summarised below.

2.1 Boundary conditions

The general boundary conditions are (Cathles 1975; Wu 2004):

(i) at the surface of the Earth, $[\tau_{rr}]_{r=0}$ = -σg_0, where σ is the surface mass density of the ice load, and r is the depth, where $r = 0$ corresponds to the surface and is defined positive downwards. In other words, the normal stress at the surface is equal to the applied pressure due to the load. For shear stresses, we have $[\tau_{r\theta}]_{r=0}$ = 0.

(ii) At internal boundaries, there should not be a discontinuity in the stress and the displacements. For the stress this implies $[\tau_{rr}]_{r-}^{r+}$ = $[\tau_{r\theta}]_{r-}^{r+}$ = 0, and for the displacement this translates to $[\mathbf{u}]_{r-}^{r+}$ = 0.

(iii) At the Core-Mantle Boundary (CMB), the fluid core is simulated by setting the normal stress equal to the multiplication of the core density, ρ_f, with gravity, g_0, and with the radial displacement at the CMB, u_r: $[\tau_{rr}]_{r=-H}$ = $\rho_f g_0 u_r$. Here H is the depth to the CMB. In Abaqus, the core is simulated by employing a Winkler foundation at the model bottom with a magnitude equal to $\rho_f g_0$. The tangential stresses vanish at the CMB, and there is continuity of displacement, i.e. $[\mathbf{u}]_{r-}^{r+}$ = 0.

2.2 The EF method

Here, we briefly review the method that uses elastic foundations and a stress transformation (Wu 2004). The setup of the model is illustrated in Figure 1a. Abaqus differentiates between small-displacement and large-displacement analyses (Table 1) via the non-linear geometry keyword (NLGEOM; Abaqus 2021 documentation, Hibbitt et al. 2016). The elements in a small-displacement analysis used by Wu (2004) do not carry the information of the stress with them. Therefore, buoyancy forces associated with density changes are not included in the stiffness matrix. Moreover, the stiffness matrix is linear, as there is no dependence on the prior displacement. Using this method, we need to manually add an isostatic restoring force to prevent the load from sinking indefinitely (Wu 1992; Purcell 1998). To still satisfy the equation of motion (equation 1), the following stress transformation is performed (Wu 2004):

$$\boldsymbol{t} = \boldsymbol{\tau} - \rho_0 g_0 u_r \boldsymbol{I}. \tag{4}$$

Here $\boldsymbol{\tau}$ is the stress, $\boldsymbol{t}$ the transformed stress, and u_r the displacement in the radial direction. The divergence of the transformed stress now becomes equal to the divergence of the stress plus the isostatic restoring force term:

$$\nabla \cdot \boldsymbol{t} = \nabla \cdot \boldsymbol{\tau} - \rho_0 g_0 \nabla u_r. \tag{5}$$

The equation of motion for non-self gravitating incompressible models reads

$$\nabla \cdot \boldsymbol{\tau} - \nabla \left(\mathbf{u} \cdot \rho_0 g_0 \hat{r} \right) = 0. \tag{6}$$

Equation 6 is the same as Equation 1, but without internal buoyancy (third term in Equation 1) and self-gravity (fourth term in Equation 1). With the stress transformation of Equation 5, we can write the equation of motion for non self-gravitating incompressible models as

$$\nabla \cdot \boldsymbol{t} = 0, \tag{7}$$

which can then be solved by Abaqus. The boundary conditions are changed because of the stress transformation, and are listed in the next subsection.

2.2.1 Boundary conditions for the EF method

The boundary conditions for the transformed stress are as follows (Wu 2004):

(i) at the surface of the Earth, $[t_{rr} + \rho_0 g_0 u_r]_{r=0}$ = -σg_0. This is the same as before, but now with an extra term due to the substitution of $\boldsymbol{t}$ for $\boldsymbol{\tau}$. The boundary conditions for the shear stresses are not affected by the stress transformation: $[\tau_{r\theta}]_{r=0}$ = 0.

(ii) at internal boundaries, we again need continuity in the stress and displacement. For the normal stress we obtain $[t_{rr}]_{r-}^{r+}$ = $(\rho_- - \rho_+)\, g_0 u_r$. For the shear stress and the displacement, we have $[\tau_{r\theta}]_{r-}^{r+}$ = 0, and $[\mathbf{u}]_{r-}^{r+}$ = 0.

(iii) at the CMB, the boundary condition is also altered, as now the difference in density between the solid lower mantle, ρ_s and the fluid core, ρ_f, is the required quantity (Wu 2004): $[t_{rr}]_{r=-H}$ = $(\rho_f - \rho_s)\, g_0 u_r$. Again, the tangential stresses vanish at the CMB, and $[\mathbf{u}]_{r-}^{r+}$ = 0.

These boundary conditions are satisfied by applying elastic foundations at the boundaries with a magnitude equal to the density difference ($\Delta\rho$) across the layer multiplied with the background gravity g_0. The elastic foundations act as a stabilizing force, as they work in the direction opposite to the radial displacement, and their magnitude increases with the radial displacement. The elastic foundations only work for horizontal boundaries, while inclined boundaries can be simulated using springs (Schmidt et al. 2012). The drawback of the EF method is that it is not possible to adapt the model to allow for compressibility (Bängtsson & Lund 2008) as the internal buoyancy force is not represented in the stiffness matrix.

2.3 The NG method

The second approach was described by Hampel et al. (2019) using the 'geometrically non-linear formulation' (N) in Abaqus and also explicitly applying a gravitational force (G), which we will label as NG. This approach has been used in studies on the interaction between ice caps and faults (e.g., Hampel & Hetzel 2006; Turpeinen et al. 2008; Hampel et al. 2009).

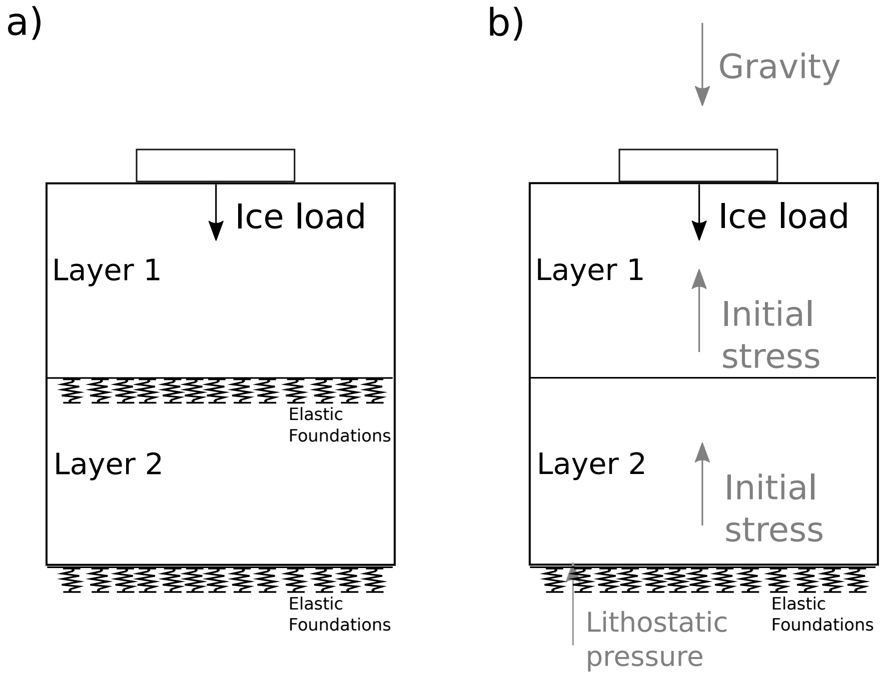

Figure 1. Schematic of a) the EF, and b) the NG model approaches. In grey are the forces and stresses specific to the NG approach.

A complete description of how Abaqus solves the governing Equations is shown in Section 1 of the Supplementary material. In the current Section, we start with the finite-element formulation of the momentum equilibrium, Equation S.10, and solve for the nodal displacements by employing Newton's method. At iteration increment k, the nodal displacements $\widetilde{u}_M^k$ are assumed and the residual, $R_N(\widetilde{u}_M^k)$, is calculated, where R_N is equal to the left hand side of equation S.10. If the

Table 1. The differences between the NG and EF methods within Abaqus, see also schematic Figure 1

Method	Non-linear geometry with Gravity (NG)	Elastic Foundations (EF)
Forces	Ice load, Gravity	Ice load
Initial stress applied	Yes	No
Spin-up steps:	1. Static step (w/ gravity only)	-
	2. Viscous step (w/ gravity only)	-
Ice loading steps:	3. Static step (w/ ice load & gravity)	1. Static step (w/ ice load)
	4. Viscous step (w/ ice load & gravity)	2. Viscous step (w/ ice load)

residual is larger than a tolerance value, the residual is calculated again for a new increment: $\widetilde{u}_M^{k+1} = \widetilde{u}_M^k + \delta\widetilde{u}_M$. Here $\delta\widetilde{u}_M$ is calculated as follows (Nguyen & Waas 2016):

$$\delta\widetilde{u}_M = -\left(\frac{\partial R_N}{\partial\widetilde{u}_M}\right)^{-1} R_N(\widetilde{u}_M^k) = -K_{NM}^{-1} R_N(\widetilde{u}_M^k). \tag{8}$$

Thus, for the Newton method used in a non-linear analysis of Abaqus, the Jacobian, $\frac{\partial R_N}{\partial\widetilde{u}_M}$, of the FE equations is considered (Hibbitt et al. 2016). This Jacobian is the stiffness matrix K_{NM}, which is sum of the stiffness matrix for the small-displacement analysis that is given by equation S.13, K_{NM}^0, the initial stress matrix, K_{NM}^σ, and the load stiffness matrix, K_{NM}^L:

$$K_{NM} = K_{NM}^0 + K_{NM}^\sigma + K_{NM}^L. \tag{9}$$

The initial stress matrix is based on the current state of stress:

$$K_{NM}^\sigma = \int_{V_0} \boldsymbol{\tau}^c : \partial_N \boldsymbol{\beta}_M dV_0, \tag{10}$$

where $\boldsymbol{\tau}^c$ is the conjugate of the stress, and $\boldsymbol{\beta}_M$ the strain-displacement matrix. The load stiffness matrix is

$$K_{NM}^L = -\int_S \mathbf{N}_M^T \cdot \mathbf{Q}_N^S dS - \int_V \mathbf{N}_M^T \cdot \mathbf{Q}_N^V dV. \tag{11}$$

The two terms on the right hand side of equation 11 are the surface and volume load stiffness matrices, respectively. They include $\mathbf{Q}_N$, the variation of the surface and volume load vectors with the nodal variables, pre-multiplied by the transpose of the interpolation functions $\mathbf{N}_M$.

In short, Abaqus describes the basic FE equations in integral form using a stiffness matrix to describe the divergence of stress (first term in equation 1), an initial stress matrix for the stress-stiffening effects (i.e. to include buoyancy, second term in equation 1), and a load stiffness matrix for the dependence of gravity loading on the current density (i.e. to calculate the internal buoyancy, the third term in equation 1). The initial stress matrix and load stiffness matrix are only included in a non-linear analysis (Abaqus keyword NLGEOM, Hibbitt et al. 2016). The procedure is non-linear as the stiffness matrix is now dependent on the displacement within the model.

Gravity loading needs to be applied explicitly to each layer (Table 1) for the correct calculation of the initial stress matrix (equation 10) and the load stiffness matrix (equation 11). As input for the gravity, we only need the value of the gravitational acceleration in the respective layer, and the associated changes in density are calculated automatically (Freed et al. 2014). An initial stress and a lithostatic pressure are applied to prevent any model displacements to take place due to the gravity loading (Figure 1b) as in Hampel et al. (2019). For our multi-layer model, the initial stress in each layer is equal to the weight of the overlying layers:

$$\sigma_{N+1} = \sum_{i=0}^{N} \rho_i g_i h_i, \tag{12}$$

with N the number of the layers, where $i = 0$ is the surface layer, and i increases for deeper layers. ρ_i, g_i, and h_i are the density, gravity, and thickness of the ith layer, respectively. For the uppermost layer ($i = 0$): $\sigma_0 = 0$. A lithostatic pressure is needed at the bottom of the model to simulate the initial stress in the core, which is calculated in the same way. An elastic foundation is present at the core-mantle boundary.

The usage of the NG approach requires two so-called spin-up steps before we apply an ice load (see Table 1 and Hampel et al. (2019)). This is necessary to obtain a stable pre-stressed equilbrium configuration. First we run a static step, in which only elastic behaviour is considered. In this step, the gravity balances the initial stress to minimize residual displacements. Following Hampel et al. (2019), we then run a viscous step of 10 thousand years (ka). After these two spin-up steps, an ice load is added and the loading scenario is performed. The run time of this approach is 5-10 min longer than a similar simulation that uses the EF approach, which does not require spin-up steps, on a total simulation time of 4-5 hours.

3 BENCHMARK SETUP

We use a spherical GIA model, labeled as SM, based on the normal mode method (NMM) for validation of the implementation of the FE models for radially symmetric Earth models. The SM model and the benchmark setup, i.e. the ice load and the Earth rheology and structure, are explained next. We identified 5 contributions for variations between the model results: (1) the difference in approach of the finite-element method (NG or EF), (2) the presence of sphericity, (3) the inclusion of self-gravity, (4) the different Earth models in the compressible runs, and (5) the approximation introduced by the FE method in general, which is controlled by the spatial resolution. Of these, contributions (4) and (5) are expected to have only a minor effect, and thus they are only briefly discussed in Sections 3.3 and 3.4, while the others represent the main goals of our investigation and these will be discussed in Section 4.

3.1 The normal mode model

In models that employ the Normal Mode Method (NMM), the variables are expanded in spherical harmonics and the system of differential equations is solved analytically in the spectral domain. The NMM is presented in detail in Peltier (1974) and Wu & Peltier (1982). Self-gravity is included in the NMM model, meaning that the fourth term in equation 1 is included, and equation 3 is solved (Table 2).

The NMM code we use is ICEAGE (Kaufmann 2004), described in Kaufmann & Lambeck (2000).The Green's functions represent the response functions and are derived from the viscoelastic load Love numbers determined by the code. All variables are expanded using spherical harmonics in order to solve the system of differential equations. The spherical harmonic expansion is truncated at degree 256, which corresponds to a spatial resolution of about 80 km. We tested the effect of the maximum spherical harmonic degree truncation on our results. Increasing the maximum spherical harmonic degree from 256 to 512 results in a maximum difference in horizontal deformation of only 0.01 m, situated around the ice edge (Supplementary Figure 1). As the original displacements are several tens of meters in the horizontal, this effect is deemed insignificant. An overview of the models employed in this study is shown in Table 2.

3.2 The loading scenarios

Here we describe the loading scenario in the experiment to validate the method of Hampel et al. (2019) for cartesian multi-layer models. Respective changes are discussed in Section 4.2.

Table 2. The models employed in the study, the geometry, Poisson's ratio, terms included in each model, and the Figures in which the respective models appear. The letter "I" in the model name refers to incompressible models.

Name	Coord	ν	$\rho' g_0 \hat{r}$	$\rho_0 \nabla \phi'$	Figures
SM	Spherical	Table 3	Y	Y	4a, 5, 6
SM-I	Spherical	0.5	–	–	2, 3, 4a, 6
NG	Cartesian	Table 3	Y	N	4b, 5, 6
NG-I	Cartesian	0.5	–	–	2, 3, 4b
EF	Cartesian	Table 3	N	N	4c, 5, 6
EF-I	Cartesian	0.5	–	–	2, 3, 4c, 6

An ice load similar to that in Spada et al. (2011) is used, which is a pillbox with a constant thickness of 1,000 m and a fixed radius. We employ discs with five radii between 222 and 1,111 km, in 222-km steps, to test the effect of the extent of the ice sheet on the accuracy of the cartesian model. This is equivalent to roughly 2 to 10 latitudinal degrees, in 2-degree steps, respectively. The density of the ice is 931 kg/m^3. The load is applied instantaneously to the model (after the necessary spin-up in case of the NG model), after which a simulation is run for 10 ka during which the load remains on the model. The displacement results are evaluated after 10 ka of loading, to agree with the benchmark studies of Spada et al. (2011) and Martinec et al. (2018).

The models are all benchmarked for the disc load example with the respective Earth model of Spada et al. (2011) in Section 3 of the supplementary material. The vertical displacements of the two FE models and SM match well with output from FastLove-HiDeg, a NMM implementation by Vermeersen & Sabadini (1997) and Riva & Vermeersen (2002) that has been benchmarked in Spada et al. (2011). Vertical displacements between FastLove-HiDeg and the respective models differ less than 3% for the 222 km radius ice load, and less than 2.5% for an ice sheet with a 1,111 km radius.

3.3 Earth model

The Earth model employed in the following experiments is determined by what we can employ in the compressible SM model. The ICEAGE code requires a high resolution of material parameter variations to suppress the growth of unstable Rayleigh-Taylor modes (Plag & Jüttner 1995; Hanyk et al. 1999; Vermeersen & Mitrovica 2000) that may occur due to unstable density stratification induced by compressional deformation (Wong & Wu 2019). In contrast, FE methods employ a rather coarse horizontal depth model with a few material parameter changes only to reduce the number of nodes and elements. Such a model with several tens of km thick homogeneous layers of constant density and bulk modulus would result in unstable conditions in compressible SM models. We employ the Preliminary Reference Earth Model (PREM, Dziewonski & Anderson 1981) for the compressible SM, and use 8 layers with volume averages of the PREM values in all other models, including the incompressible SM (Table 3). The depths of the 8 layers are chosen to minimize the differences in the velocities due to different material-parameter layer approximations.

The presence of a density inversion in the volume averaged density profile requires a negative elastic foundation in the EF model. Hampel et al. (2019) outlined that this would be impossible in Abaqus. Indeed this cannot be done in the Abaqus/CAE frontend, but it can be done directly in the input file or by applying the foundation at the bottom face of the element above the boundary instead of the top face of the element below the boundary. As the negative density jump at 80 km is only 9 kg/m^3, we omit the use of an elastic foundation at this boundary in the EF model.

We quantified the effect of the Earth model approximation using incompressible models for the horizontal displacements and for the horizontal displacement rates in Section 4 of the Supplementary Materials. This difference will determine how well we can validate the cartesian NG model. Its effect fluctuates around 5% of the horizontal displacement for both the 222 and 1,111 km radius ice sheet, with a peak to at most 12% at the ice edge for the larger ice sheet. For the horizontal displacement rates, the effect is a bit less than 10% below the ice load, decreasing to 5% just outside of the ice edge.

3.4 Resolution in the finite element models

The resolution selected in the FE model is a trade-off between accuracy and computation time. The vertical resolution is only 1 km in SM. In the FE models, it is not feasible to use as many layers. We ran several resolution tests and find that the results are most sensitive to the horizontal

Table 3. The Earth model parameters for the 8 layer configuration. Values are volume averages derived from PREM. The depth is defined positive downwards.

Layer	From (km)	To (km)	Density (kg/m^3)	Young's modulus ($\times 10^{12}$ Pa)	Viscosity ($\times 10^{21}$ Pa s)	Gravity (m s^{-2})	Poisson's ratio
1	0	25	2,895.7506	0.1091	–	9.8356	0.2638
2	25	80	3,376.7141	0.1721	–	9.8499	0.2803
3	80	220	3,365.9506	0.1638	1	9.8862	0.2874
4	220	400	3,501.3442	0.1981	1	9.9424	0.3000
5	400	670	3,910.8079	0.2858	1	9.9968	0.2960
6	670	2,891	5,215.9378	0.6590	2	10.1826	0.2974
7	2,891	5,149.5	10,750	0	0	7.1302	0.5000
8	5,149.5	6,371	13,000	0.4721	0	2.0626	0.4437

resolution. Differences are less than 1 m between a horizontal resolution of 27 and 54 km (0.25 and 0.5 lateral degrees, respectively). We therefore opt for a horizontal resolution of $\sim$27 km and do not aim for a higher horizontal resolution. Furthermore, each of the 8 Earth layers is divided into 4 FE layers in the vertical direction. We use this resolution in the region covering the inner 2,200 km of the model. The total width of the model is 20,000 km, and the outer region has a coarser resolution of $\sim$550 km (5 degrees in lateral extent). This setup with a higher resolution in the region below and close to the ice sheet is similar to the setup of the cartesian models in Schotman et al. (2008) and Marsman et al. (2021). Using 16 cores, a computation time is achieved of roughly 4-4.5 hours for the incompressible and material compressible simulations, and 4.5-5 hours for the compressible NG runs. We make use of hexahedral, 8 node elements of type C3D8H for the incompressible models and C3D8 for the compressible models (including models using material compressiblity).

4 RESULTS

Hampel et al. (2019) showed that the NG method works for incompressible homogeneous half space models and for incompressible shallow (i.e. 100 km deep) cartesian models consisting of two layers. In principle, the NG method is suitable to deal with compressibility, and this was tested for the shallow two layer cartesian models (Hampel et al. 2019). To allow the usage of the method to model glacial loading scenarios, the model needs to include a lithosphere and the mantle down to the core-mantle boundary. We extend their model to the core of the Earth by incorporating the 8-layer approximation, and make the model compressible by changing Poisson's ratio to the values listed in Table 3. We apply a disc load of 1,111 km (as described in Section 3.2), and compare the horizontal displacement of the NG and EF models against results from SM to understand the differences.

We distinguish three forms of compressibility: (1) full compressibility including the effect of compressibility on self-gravity in equation 3, (2) full compressibility without self-gravity, and (3) material compressibility (Klemann et al. 2003). The full compressible models differ from the material compressible model in that they include the internal buoyancy force in the equation of motion (equation 1). The compressible version of SM simulates (1), NG reproduces (2), and EF can only include (3).

4.1 Displacements

4.1.1 Incompressible model results

First, we investigate three effects mentioned at the start of Section 3: the approach taken by the FE method, sphericity, and self-gravity. We isolate the first effect by comparing results from the EF-I and NG-I models. Comparing these cartesian models with SM then gives us the combined effect of the second and the third. Amelung & Wolf (1994) noted that self-gravity compensates for the sphericity in the vertical. We examine if such a compensation is also present in the horizontal.

Horizontal displacements underneath and outside of the ice sheet are positive (outwards) after 10 ka of loading with a 1,111 km radius ice sheet for all models, with a (local) minimum at the ice sheet boundary (Figure 2). During loading, the mantle flow is outwards from the center of loading resulting in positive displacements, while lithospheric flexure results in a motion towards the center of the ice sheet (O'Keefe & Wu 2002). Horizontal lithospheric flexure is largest at the ice sheet boundary, explaining the location of the (local) minimum. The maximum value of the horizontal displacement is found outside of the ice sheet, and ranges from 20 m for NG-I and

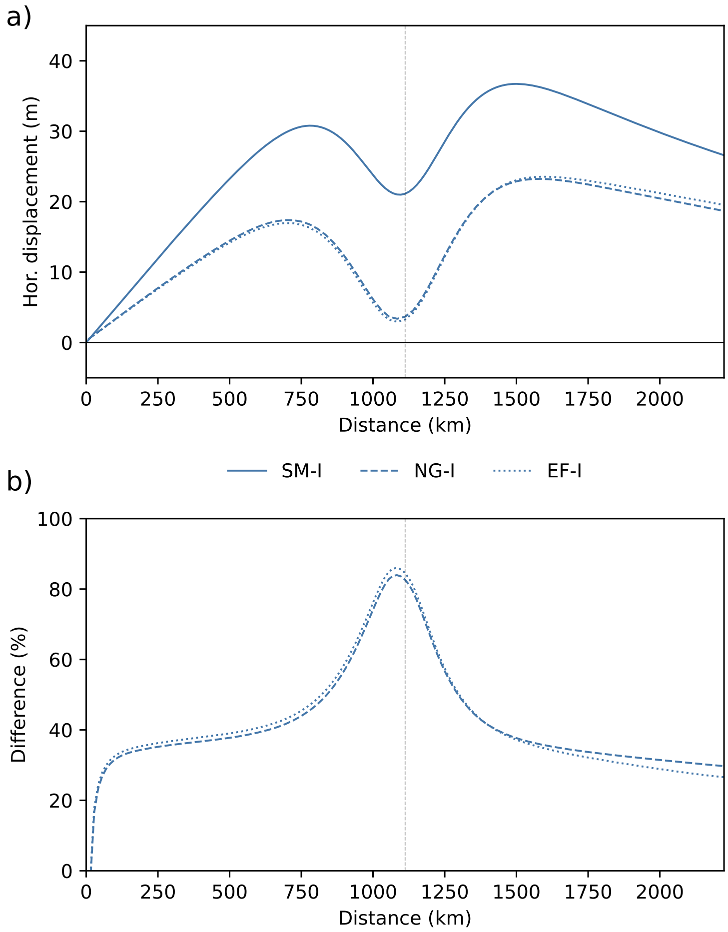

Figure 2. Horizontal displacement after 10 ka of loading using an ice load 1,111 km in radius for (a) SM-I, NG-I, and EF-I, and (b) the difference in percentage of NG-I and EF-I with SM-I. The edge of the ice load is marked by a vertical grey dashed line.

EF-I to more than 35 m for SM. Overall, the cartesian models EF-I and NG-I are found to be in excellent agreement, especially in the near field (Figure 2a). Therefore, we conclude that the approach taken by the FE method only leads to insignificant changes using a complete Earth model from the surface of the Earth down to the core-mantle boundary.

To investigate the effect of sphericity and self-gravity we compare the cartesian models with SM in Figure 2b. We observe a significant difference in simulated horizontal displacement of about 40% below the load, increasing to more than 80% at the load edge (Figure 2b). Thus, where self-gravity partially compensates for the sphericity in the vertical (Amelung & Wolf 1994), this is not the case for the horizontal. In the next Section we test if a better agreement can be obtained using a smaller ice sheet, which minimises the effects of self-gravity (Pollitz 1997) and sphericity.

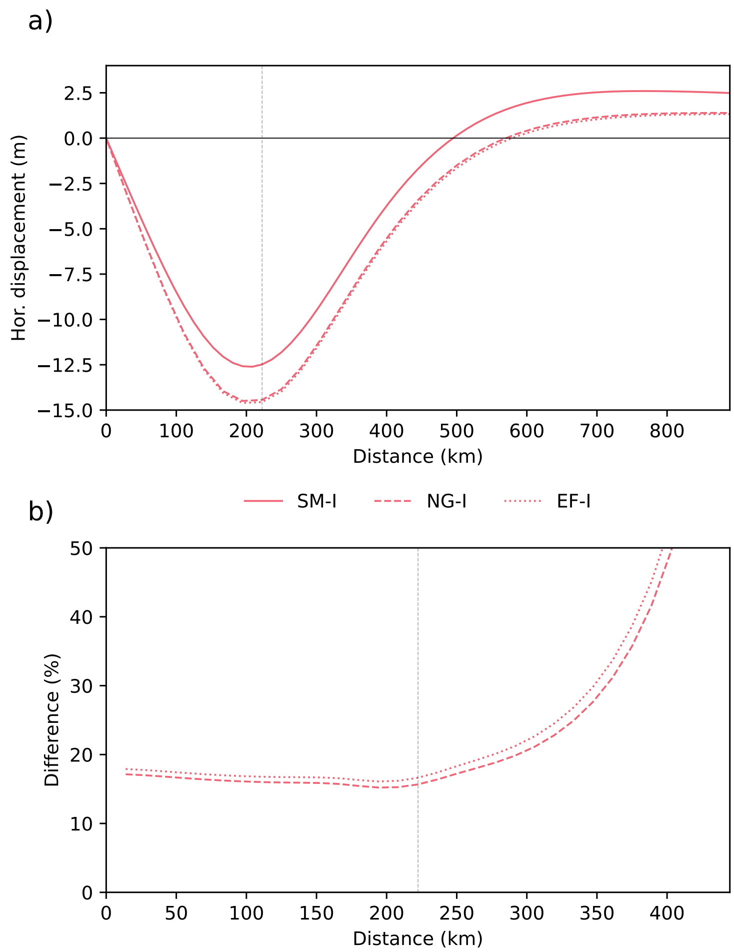

Figure 3. a) Horizontal displacement after 10 ka of loading as simulated by SM-I, NG-I, and EF-I, and b) the difference of NG-I and EF-I with SM-I. The dashed and dotted lines are on top of each other in Figure a. The edge of the ice load is marked by a vertical grey dashed line.

4.1.2 Displacements for a small ice sheet

With an ice sheet 222 km (2 degrees) in radius, the modelled horizontal displacements are inwards below the ice sheet. This is a result of the lithospheric flexure that is dominant for an ice sheet with a small lateral extent. The displacements are smaller in magnitude, and only -15 m at most (Figure 3a). Differences between the incompressible cartesian and spherical models are less than 20% below the load (Figure 3b). For such a small ice sheet, the agreement between cartesian and spherical models has significantly improved compared to the largest ice sheet of this study.

4.1.3 The effect of compressibility on the displacements

To understand the effect of the different approximations for compressibility, we compare the incompressible and compressible simulations. In all models, the effect is most pronounced at the ice margins, which is also illustrated by the volumetric strain in Section 6 of the Supplementary Materials that shows the dilatation of the elements and is thereby a measure of the relative magnitude of compressibility. An increasing effect is seen for larger ice sheets in SM and NG, but not for EF (Figure 4). Evidently, including the internal buoyancy force leads to an increasing effect below and further outside the load. For the smallest ice sheet, the effect of compressibility in NG and SM is circa 5 and 6 m, respectively (on a total deflection of 20-40 m). For larger ice sheets, this effect increases to almost 25 m in both models. The resulting compressibility effect of SM and NG agrees to a large extent, but also exhibits minor differences, which are caused by the different Earth model and by the resolution, possibly combined with the effect of self-gravity on compressibility which is included in SM but not in NG.

The effect of material compressibility on the horizontal displacement for EF is at most 3-4 m, independent of the size of the ice sheet (Figure 4c). Its effect peaks around the ice edge, where the density change due to deformation is largest (Figure S7). This is also where the flexure in the lithosphere is largest as this is where the slope in the vertical displacement is at its maximum. For small ice sheets, the material compressible EF model performs similar to the other compressible models. However, as the size of the ice sheets increase, the agreement deteriorates. Based on Figure 4, we conclude that material compressibility only approximates compressibility for small ice sheets, although NG outperforms EF even for such small ice sheets.

4.1.4 Compressible model results

With all the information from the previous Section we are now able to explain Figure 5 which shows the horizontal displacement of compressible and material compressible models after 10 ka of loading with an ice sheet 1,111 km in radius. Differences with respect to SM are smaller for EF (mostly less than 15% below the load) than for NG (50% almost everywhere, Figure 5b). The approximation of compressiblility as material compressibility in EF leads to a decent agreement

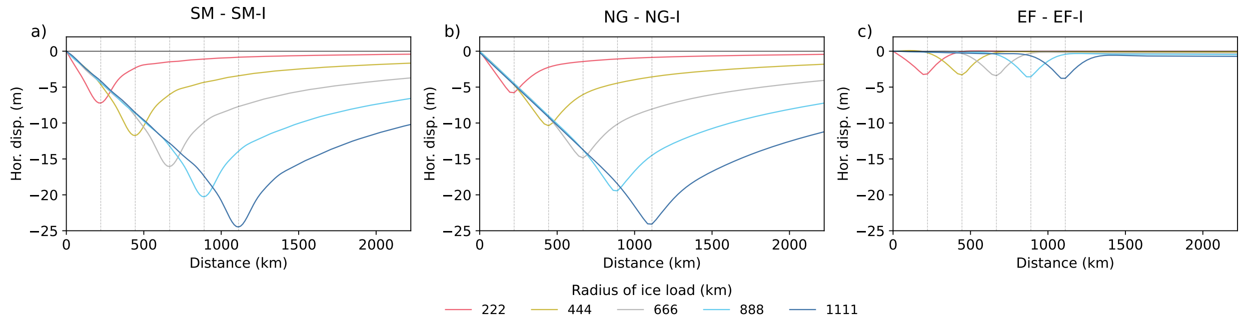

Figure 4. The effect of compressibility on the modelled horizontal displacements in (a) SM, (b) NG, and (c) EF. SM-I uses the PREM Earth model, just like SM. The edges of the ice loads are marked by vertical grey dashed lines.

with the spherical model. The lack of full compressibility in this approximation partly compensates for the lack of sphericity, leading to a better apparent agreement even though compressibility is modelled less accurately. Furthermore, we notice that for the 222 km radius ice sheet NG indeed matches the SM results better than EF (Figure 5c). The advantage of NG simulating compressibility better than EF is unfortunately diminished by the effect of sphericity, and thus the NG approach is less applicable for modelling large ice sheets.

4.2 Horizontal displacement rates

The total horizontal displacement due to GIA cannot be observed, while the rate in horizontal displacement (the velocity) can be measured using Global Navigation Satellite Systems (GNSS) stations. Therefore we focus on the rates in the remainder, and assess the magnitude of modelling approximations.

We aim to develop a case study that is representative for GIA in Iceland, Alaska, and NAP. Based on studies of those regions (e.g., Pagli et al. 2007; Árnadóttir et al. 2009; Elliott et al. 2010; Nield et al. 2014; Hu & Freymueller 2019), we select an elastic thickness of 80 km, and between 80 km and 220 km we consider a low viscosity layer of 1×10^{19} Pa s. Below this layer down to 670 km, we employ an upper mantle viscosity of 4×10^{20} Pa s, the same value as in Fleming et al. (2007), Larsen et al. (2005), and Elliott et al. (2010). The lower mantle viscosity (below 670 km) is 1×10^{22} Pa s. The ice load has a radius of 222 km, just as before in this paper. Due to the small

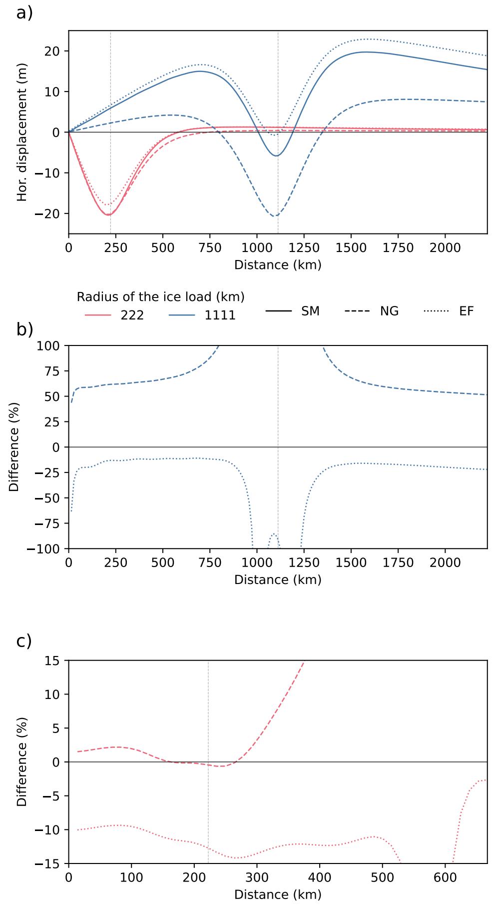

Figure 5. (a) Horizontal displacement after 10 ka of loading using ice loads 1,111 and 222 km in radius for SM, NG, and EF, as well as the difference of NG and EF with SM for (b) the 1,111 km and (c) 222 km radius ice sheets. The edges of the ice loads are marked by vertical grey dashed lines.

extent of the load, GIA is mainly sensitive to the upper layers, and the exact value of the lower mantle viscosity is less important (Fleming et al. 2007; Sato et al. 2011). We employ the PREM Earth model values for both incompressible and compressible SM simulations, and a layered Earth model with volume averages in the cartesian models. The thickness of the ice cap has been tuned so that the modelled vertical rates match the peak uplift rates observed in Alaska of $30-35$ mm/a (Larsen et al. 2005). A good fit has been found for an ice cap thickness of 200 m.

To start, we simulate 2 ka of loading. Fleming et al. (2007) concluded that the influence of Last-Glacial Maximum ice loads was negligible over Iceland. In combination with the low viscosity profile employed, we deem 2 ka of loading to be sufficient to reach equilbrium for our case studies. We will assume equilibrium with the load prior to unloading, and then calculate the displacement rates after 205 years of unloading. The rates are calculated as the difference between 200 and 210 years after unloading, divided by 10 years. We use a spin-up of 10 ka in the NG simulations as described in Section 3.2, although we expect that this could be shorter (e.g. 2 ka) due to the presence of a low viscosity layer in that simulation. The runtime is 3-3.5 hours for the incompressible simulations, and 6-6.5 hours for the compressible NG run. In SM, runtimes are only a few seconds.

Modelled horizontal displacement rates reach values of 5-7 mm/a, similar to those modelled by Elliott et al. (2010) for Alaska. The largest displacement rates of up to 6.8 mm/a are found for SM (Figure 6a.). We use SM as a reference, and compare it with all other models in Figure 6b. The effect of compressibility on the horizontal can be seen by comparing SM and SM-I, and amounts to about 1.5 mm/a at most, again showing that the effect of compressibility is not negligible in the horizontal (James & Lambert 1993; Mitrovica et al. 1994; Tanaka et al. 2011).

The cartesian models all simulate displacement rates that differ less than 1.1 mm/a from SM (Figure 6b). Differences are 0.93 mm/a for the EF model, and 0.63 mm/a for the NG model. However, the maximum in the difference to the EF model has also moved in the horizontal direction (it is now outside the load). This model nevertheless provides a minor improvement with respect to EF-I, although no as much as the NG model.

These modelling technique-dependent differences can still be considered significant when compared to current precision and uncertainties of GNSS observations. Kierulf et al. (2021) show that horizontal velocities of GNSS networks can reach such precision already after 2-3 years of observations. Uncertainties of horizontal velocities meanwhile reach 0.5 mm/a for global GNSS solutions (Vardić et al. 2022) and, depending on the chosen noise model and further corrections, can be much less than 0.35 mm/a for regional ones (Lahtinen et al. 2019; Kierulf et al. 2021).

5 STEPS TOWARDS A COMPRESSIBLE SPHERICAL FINITE ELEMENT MODEL

Modelling the whole GIA process eventually requires including sea-level changes induced by the ice mass changes and the deformation, and their effect on deformation itself. Such interactions must be solved on a global scale with a spherical model. This spherical model should

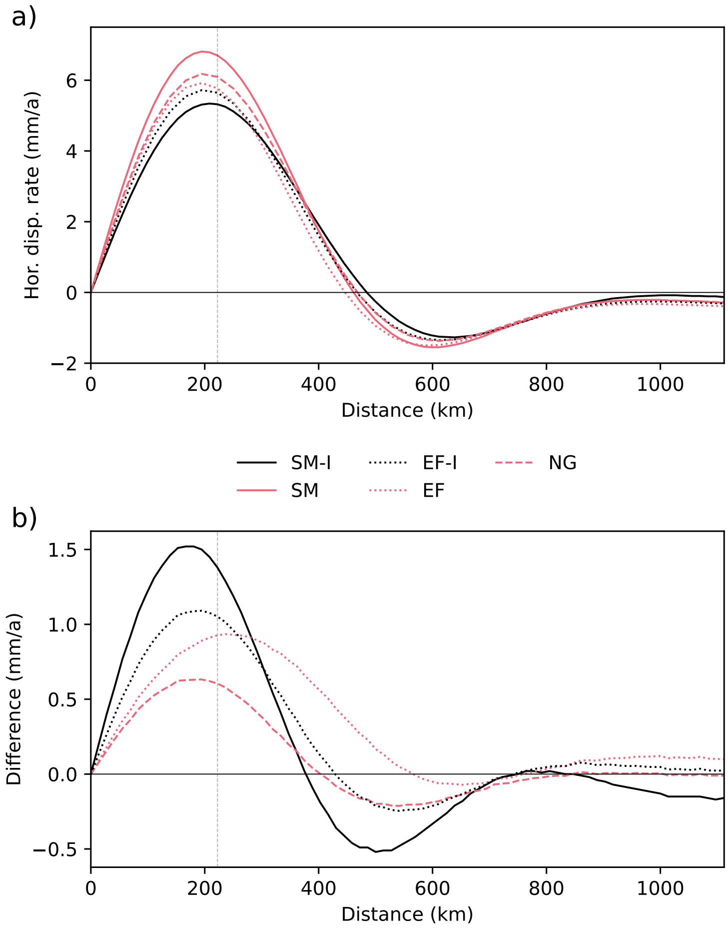

Figure 6. Horizontal displacement rate for (a) SM, SM-I, NG, EF, and EF-I, and (b) differences of the respective models with SM. The edge of the ice load is marked by a vertical grey dashed line.

ideally allow the implementation of lateral heterogeneous material parameters. Several fully or partially compressible spherical 3D models have already been developed. Latychev et al. (2005) implemented compressibility in a 3D GIA model, but only elastic compressibility was included. Martinec (2000) developed a spectral finite-element model for 3D visco-elastic relaxation in a spherical Earth, which was extended by Tanaka et al. (2011) to allow for compressibility. A 3D finite-element (FE) model by Zhong et al. (2003) was ameliorated by A et al. (2013) to achieve a fully compressible 3D FE model. Wong & Wu (2019) introduced a new approach by calculating separately the change in body forces due to compressibility in iteration with the FE model. However, their approach is not yet applicable for realistic loadings.

As the NG method is able to represent the compressible effects in a straight-forward way, we try to implement the NG method in spherical FE models. However, the limiting factor turns out to be the explicit application of gravity loading. Gravity can be defined in the vertical direction for a cartesian model, but Abaqus does currently not have the option for gravity to be directed radially inward as is the case for a spherical body. Gravity can of course be implemented separately as a body force that is directed radially inward, but for the magnitude of the body force we need to manually compute the density, which changes as a result of compressibility (third term in equation 1). In principle, we can calculate the dilatation and the corresponding density change for every time step and iterate. If we were to do this, we lose the advantage of the NG method, namely that Abaqus includes the load stiffness matrix (equation 11), and thereby automatically considers changes in density associated with changes in pressure (Freed et al. 2014). We suggest that, for complete simulations for a compressible spherical model, approaches such as those in Wong & Wu (2019) should be used, who solve the differential equations iteratively and apply the change in body force due to compressibility.

6 CONCLUSION

Cartesian models of Glacial Isostatic Adjustment (GIA) previously generated by Abaqus have neglected compressibility. Here, we extended a method for including compressibility in FE models using a geometrically non-linear formulation with explicit application of gravity (Hampel et al. 2019), named NG. The method has the advantage that it includes compressibility in line with the GIA equation of motion. Compressibility (without self-gravity) is accounted for including the effect of dilatation on buoyancy forces when we decrease Poisson's ratio below that of incompressible materials. We investigated the effect of two assumptions made in earlier studies, namely incompressibility and a cartesian Earth model (e.g., Ivins & James 1999; Larsen et al. 2003, 2004; Pagli et al. 2007; Schotman et al. 2008; Árnadóttir et al. 2009; Zwinger et al. 2020). We also investigate material compressibility in the conventional method (e.g., Kaufmann et al. 2005; Steffen et al. 2006; Lund et al. 2009; Auriac et al. 2013; Nield et al. 2018; Marsman et al. 2021), which allows for material compression, but does not include the internal buoyancy force in the equation of motion. The conventional method has been named as EF.

We considered the spherical normal mode model SM to simulate the full effect of compressibility, and tested the effect of compressibility and material compressibility in the FE models NG and EF against it. The absolute effect of compressibility on the horizontal displacement is most evident at the ice margins, and increases for larger ice sheets in SM and NG. The effect of compressibility in the material compressible EF model shows no dependence on the size of the ice sheet, which indicates that compressibility is not represented well. For ice sheets below roughly 200 km in radius, only considering material compressibility in the constitutive equation (Hooke's law) is a reasonable approximation of full compressibility, although NG performs better even for small ice sheets. At the same time sphericity is found to be important for simulations that aim to model the horizontal displacement rates, and it can only be neglected for small (maximum $\sim$200 km radius) ice sheets. While sphericity and self-gravity at least partly compensate each other in the vertical, we find that there is no such compensation for horizontal displacements. For larger ice sheets, horizontal displacements simulated by material compressible EF models perform better than compressible NG models as the missing full compressibility is partly compensated with the lack of sphericity.

We investigated the applicability of the cartesian models in small scale GIA studies with large uplift rates due to recent unloading by simulating the horizontal displacement rates for a scenario representative for post-LIA uplift in Iceland, Alaska, and West Antarctica. Horizontal displacement rates of compressible and material compressible cartesian models differ from SM by 0.63 and 0.93 mm/a, for NG and EF respectively. SM-I differs by 1.5 mm/a, and therefore performs worse than the cartesian models, highlighting the importance of using compressibility for modelling horizontal velocities of small-scale GIA. To conclude, we show that for small ice sheets results from cartesian models are sufficiently close to results when the full GIA equation of motion (including self-gravity) is solved, and the compressible cartesian NG model approach is acceptable (Table 4).

Since most GNSS observations are available for long time spans even in such small-scale regions like Alaska, Iceland and NAP, the appropriate modelling approach has to be chosen before a comparison of modelled vs. observed horizontal velocities can be made. We see that for an ice sheet with a 222 km radius, the accuracy of the NG model is slightly above any GNSS precision

Table 4. An overview of the models in this study, where they are applicable and their computation time. The values for the differences with SM are shown below the load for the compressible and material compressible simulations for NG and EF, respectively.

Name	Coord	Can lateral variations be included?	Approximate computation time	Difference with SM (2 deg radius load)	Difference with SM (10 deg radius load)
SM	Spherical	N	$\sim$ seconds to few minutes	-	-
NG	Cartesian	Y	3-3.5 hours (incompressible) Up to 6.5 hours (compressible)	hor disp: <2.5% rate: 0.63 mm/yr	hor disp: >50%
EF	Cartesian	Y	3-3.5 hours (material compressible and incompressible)	hor disp: 10-15% rate: 0.93 mm/yr	hor disp: <25 %

and uncertainty. Hence, only smaller ice caps should be modelled with cartesian NG models when fitting horizontal velocities is the goal.

Horizontal displacement rates are sensitive to mantle viscosity, and much can be learned from investigating them in small scale study areas like Alaska, Iceland, or West Antarctica (e.g., Árnadóttir et al. 2009; Samrat et al. 2020; Marsman et al. 2021). We tested the effect of compressibility in 1D models, but the cartesian models can accomodate 3D subsurface structures that are likely to exist. Finally, we attempted to implement the NG method in a spherical FE model, but found that the advantage of this method is lost, as a radial gravity distribution cannot be specified in Abaqus. Therefore, the change in buoyancy forces would have to be calculated outside the FE software as done by e.g. Wong & Wu (2019), conform the finding of Bängtsson & Lund (2008) that it is impossible to calculate the buoyancy force inside the FE software.

ACKNOWLEDGMENTS

We thank the editor Duncan Agnew, and Volker Klemann and one anonymous reviewer for the constructive comments which helped to improve the manuscript. We wish to acknowledge Pingping Huang for insightful discussions. This research was (partially) funded by NWO Science domain (NWO-ENW), project ALW.GO.2017.035. RS is supported by a project grant from Rymdstyrelsen (Swedish National Space Agency; grant number 2018-00140).

DATA AVAILABILITY

The input files for the Abaqus models and the horizontal outputs of the ICEAGE runs are made available at the 4TU data repository: https://doi.org/10.4121/9a9bdb35-8f65-41f1-be00-4d247722ad48.v1

REFERENCES

A, G., Wahr, J., & Zhong, S., 2013. Computations of the viscoelastic response of a 3-D compressible Earth to surface loading: an application to Glacial Isostatic Adjustment in Antarctica and Canada, *Geophysical Journal International*, **192**(2), 557–572.

Amelung, F. & Wolf, D., 1994. Viscoelastic perturbations of the earth: significance of the incremental gravitational force in models of glacial isostasy, *Geophysical Journal International*, **117**(3), 864–879.

Árnadóttir, T., Lund, B., Jiang, W., Geirsson, H., Björnsson, H., Einarsson, P., & Sigurdsson, T., 2009. Glacial rebound and plate spreading: results from the first countrywide GPS observations in Iceland, *Geophysical Journal International*, **177**(2), 691–716.

Auriac, A., Spaans, K., Sigmundsson, F., Hooper, A., Schmidt, P., & Lund, B., 2013. Iceland rising: Solid Earth response to ice retreat inferred from satellite radar interferometry and visocelastic modeling, *Journal of Geophysical Research: Solid Earth*, **118**(4), 1331–1344.

Backus, G. E., 1967. Converting vector and tensor equations to scalar equations in spherical coordinates, *Geophysical Journal International*, **13**(1-3), 71–101.

Bängtsson, E. & Lund, B., 2008. A comparison between two solution techniques to solve the equations of glacially induced deformation of an elastic Earth, *International journal for numerical methods in engineering*, **75**(4), 479–502.

Cathles, L. M., 1975. *Viscosity of the Earth's Mantle*, Princeton University Press.

Dziewonski, A. M. & Anderson, D. L., 1981. Preliminary reference Earth model, *Physics of the earth and planetary interiors*, **25**(4), 297–356.

Elliott, J. L., Larsen, C. F., Freymueller, J. T., & Motyka, R. J., 2010. Tectonic block motion and glacial isostatic adjustment in southeast Alaska and adjacent Canada constrained by GPS measurements, *Journal of Geophysical Research: Solid Earth*, **115**(B9).

Fleming, K., Martinec, Z., & Wolf, D., 2007. Glacial-isostatic adjustment and the viscosity structure underlying the Vatnajökull Ice Cap, Iceland, in *Deformation and Gravity Change: Indicators of Isostasy, Tectonics, Volcanism, and Climate Change*, pp. 751–768, Springer.

Freed, A. M., Johnson, B. C., Blair, D. M., Melosh, H., Neumann, G. A., Phillips, R. J., Solomon, S. C., Wieczorek, M. A., & Zuber, M. T., 2014. The formation of lunar mascon basins from impact to contemporary form, *Journal of Geophysical Research: Planets*, **119**(11), 2378–2397.

Gasperini, P., Yuen, D. A., & Sabadini, R., 1990. Effects of lateral viscosity variations on postglacial rebound: Implications for recent sea-level trends, *Geophysical Research Letters*, **17**(1), 5–8.

Hampel, A. & Hetzel, R., 2006. Response of normal faults to glacial-interglacial fluctuations of ice and water masses on Earth's surface, *Journal of Geophysical Research: Solid Earth*, **111**(B6).

Hampel, A., Hetzel, R., Maniatis, G., & Karow, T., 2009. Three-dimensional numerical modeling of slip rate variations on normal and thrust fault arrays during ice cap growth and melting, *Journal of Geophysical Research: Solid Earth*, **114**(B8).

Hampel, A., Lüke, J., Krause, T., & Hetzel, R., 2019. Finite-element modelling of glacial isostatic adjustment (GIA): Use of elastic foundations at material boundaries versus the geometrically non-linear formulation, *Computers & geosciences*, **122**, 1–14.

Hanyk, L., Matyska, C., & Yuen, D. A., 1999. Secular gravitational instability of a compressible viscoelastic sphere, *Geophysical research letters*, **26**(5), 557–560.

Hermans, T., van der Wal, W., & Broerse, T., 2018. Reversal of the direction of horizontal velocities induced by GIA as a function of mantle viscosity, *Geophysical Research Letters*, **45**(18), 9597–9604.

Hibbitt, D., Karlsson, B., & Sorensen, P., 2016. Getting started with ABAQUS, version (6.14), *Hibbit, Karlsson & Sorensen, Inc*.

Hu, Y. & Freymueller, J. T., 2019. Geodetic observations of time-variable glacial isostatic adjustment in Southeast Alaska and its implications for Earth rheology, *Journal of Geophysical Research: Solid Earth*, **124**(9), 9870–9889.

Ivins, E. R. & James, T. S., 1999. Simple models for late Holocene and present-day Patagonian glacier fluctuations and predictions of a geodetically detectable isostatic response, *Geophysical Journal International*, **138**(3), 601–624.

James, T. S. & Lambert, A., 1993. A comparison of VLBI data with the ICE-3G glacial rebound model, *Geophysical Research Letters*, **20**(9), 871–874.

Johnston, P., Lambeck, K., & Wolf, D., 1997. Material versus isobaric internal boundaries in the Earth and their influence on postglacial rebound, *Geophysical Journal International*, **129**(2), 252–268.

Kaufmann, G., 2004. Program Package ICEAGE, Version 2004., Manuscript. Institut für Geophysik der

Universität Göttingen.

Kaufmann, G. & Lambeck, K., 2000. Mantle dynamics, postglacial rebound and the radial viscosity profile, *Physics of the Earth and Planetary Interiors*, **121**(3-4), 301–324.

Kaufmann, G., Wu, P., & Ivins, E. R., 2005. Lateral viscosity variations beneath Antarctica and their implications on regional rebound motions and seismotectonics, *Journal of Geodynamics*, **39**(2), 165–181.

Kierulf, H. P., Steffen, H., Barletta, V. R., Lidberg, M., Johansson, J., Kristiansen, O., & Tarasov, L., 2021. A GNSS velocity field for geophysical applications in Fennoscandia, *Journal of Geodynamics*, **146**, 101845.

Klemann, V., Wu, P., & Wolf, D., 2003. Compressible viscoelasticity: stability of solutions for homogeneous plane-Earth models, *Geophysical Journal International*, **153**(3), 569–585.

Lahtinen, S., Jivall, L., Häkli, P., Kall, T., Kollo, K., Kosenko, K., Galinauskas, K., Prizginiene, D., Tangen, O., Weber, M., et al., 2019. Densification of the itrf2014 position and velocity solution in the nordic and baltic countries, *GPS solutions*, **23**, 1–13.

Larsen, C. F., Echelmeyer, K. A., Freymueller, J. T., & Motyka, R. J., 2003. Tide gauge records of uplift along the northern Pacific-North American plate boundary, 1937 to 2001, *Journal of Geophysical Research: Solid Earth*, **108**(B4).

Larsen, C. F., Motyka, R. J., Freymueller, J. T., Echelmeyer, K. A., & Ivins, E. R., 2004. Rapid uplift of southern Alaska caused by recent ice loss, *Geophysical Journal International*, **158**(3), 1118–1133.

Larsen, C. F., Motyka, R. J., Freymueller, J. T., Echelmeyer, K. A., & Ivins, E. R., 2005. Rapid viscoelastic uplift in southeast Alaska caused by post-Little Ice Age glacial retreat, *Earth and planetary Science letters*, **237**(3-4), 548–560.

Latychev, K., Mitrovica, J. X., Tromp, J., Tamisiea, M. E., Komatitsch, D., & Christara, C. C., 2005. Glacial isostatic adjustment on 3-D Earth models: a finite-volume formulation, *Geophysical Journal International*, **161**(2), 421–444.

Li, T., Wu, P., Wang, H., Steffen, H., Khan, N. S., Engelhart, S. E., Vacchi, M., Shaw, T. A., Peltier, W. R., & Horton, B. P., 2020. Uncertainties of glacial isostatic adjustment model predictions in North America associated with 3D structure, *Geophysical Research Letters*, **47**(10), e2020GL087944.

Lund, B., Schmidt, P., & Hieronymus, C., 2009. Stress evolution and fault stability during the Weichselian glacial cycle.

Marsman, C. P., van der Wal, W., Riva, R. E., & Freymueller, J. T., 2021. The Impact of a 3-D Earth Structure on Glacial Isostatic Adjustment in Southeast Alaska Following the Little Ice Age, *Journal of Geophysical Research: Solid Earth*, **126**(12), e2021JB022312.

Martinec, Z., 2000. Spectral–finite element approach to three-dimensional viscoelastic relaxation in a spherical earth, *Geophysical Journal International*, **142**(1), 117–141.

Martinec, Z., Klemann, V., van der Wal, W., Riva, R., Spada, G., Sun, Y., Melini, D., Kachuck, S., Barletta, V., Simon, K., et al., 2018. A benchmark study of numerical implementations of the sea level equation in GIA modelling, *Geophysical Journal International*, **215**(1), 389–414.

Mitrovica, J., Davis, J., & Shapiro, I., 1994. A spectral formalism for computing three-dimensional deformations due to surface loads: 2. Present-day glacial isostatic adjustment, *Journal of Geophysical Research: Solid Earth*, **99**(B4), 7075–7101.

Nguyen, N. & Waas, A. M., 2016. Nonlinear, finite deformation, finite element analysis, *Zeitschrift für angewandte Mathematik und Physik*, **67**(3), 1–24.

Nield, G. A., Barletta, V. R., Bordoni, A., King, M. A., Whitehouse, P. L., Clarke, P. J., Domack, E., Scambos, T. A., & Berthier, E., 2014. Rapid bedrock uplift in the Antarctic Peninsula explained by viscoelastic response to recent ice unloading, *Earth and Planetary Science Letters*, **397**, 32–41.

Nield, G. A., Whitehouse, P. L., van der Wal, W., Blank, B., O'Donnell, J. P., & Stuart, G. W., 2018. The impact of lateral variations in lithospheric thickness on glacial isostatic adjustment in West Antarctica, *Geophysical Journal International*, **214**(2), 811–824.

Nield, G. A., King, M. A., Steffen, R., & Blank, B., 2022. A global, spherical finite-element model for post-seismic deformation using Abaqus, *Geoscientific Model Development*, **15**(6), 2489–2503.

O'Keefe, K. & Wu, P., 2002. Effect of mantle structure on postglacial induced horizontal displacement, *Ice Sheets, Sea Level and the Dynamic Earth, Geodyn. Ser*, **29**, 109–118.

Pagli, C., Sigmundsson, F., Lund, B., Sturkell, E., Geirsson, H., Einarsson, P., Árnadóttir, T., & Hreinsdóttir, S., 2007. Glacio-isostatic deformation around the Vatnajökull ice cap, Iceland, induced by recent climate warming: GPS observations and finite element modeling, *Journal of Geophysical Research: Solid Earth*, **112**(B8).

Peltier, W., 1974. The impulse response of a Maxwell Earth, *Reviews of Geophysics*, **12**(4), 649–669.

Plag, H.-P. & Jüttner, H.-U., 1995. Rayleigh-Taylor instabilities of a self-gravitating Earth, *Journal of geodynamics*, **20**(3), 267–288.

Pollitz, F. F., 1997. Gravitational viscoelastic postseismic relaxation on a layered spherical Earth, *Journal of Geophysical Research: Solid Earth*, **102**(B8), 17921–17941.

Purcell, A., 1998. The significance of pre-stress advection and internal buoyancy in the flat-Earth formulation, *Dynamics of the ice age earth: a modern perspective*, pp. 105–122.

Riva, R. & Vermeersen, L., 2002. Approximation method for high-degree harmonics in normal mode modelling, *Geophysical Journal International*, **151**(1), 309–313.

Samrat, N. H., King, M. A., Watson, C., Hooper, A., Chen, X., Barletta, V. R., & Bordoni, A., 2020. Reduced ice mass loss and three-dimensional viscoelastic deformation in northern Antarctic Peninsula inferred from GPS, *Geophysical Journal International*, **222**(2), 1013–1022.

Sato, T., Larsen, C. F., Miura, S., Ohta, Y., Fujimoto, H., Sun, W., Motyka, R. J., & Freymueller, J. T.,

2011. Reevaluation of the viscoelastic and elastic responses to the past and present-day ice changes in Southeast Alaska, *Tectonophysics*, **511**(3-4), 79–88.

Schmidt, P., Lund, B., & Hieronymus, C., 2012. Implementation of the glacial rebound prestress advection correction in general-purpose finite element analysis software: Springs versus foundations, *Computers & Geosciences*, **40**, 97–106.

Schotman, H., Wu, P., & Vermeersen, L., 2008. Regional perturbations in a global background model of glacial isostasy, *Physics of the Earth and Planetary Interiors*, **171**(1-4), 323–335.

Spada, G., Barletta, V. R., Klemann, V., Riva, R., Martinec, Z., Gasperini, P., Lund, B., Wolf, D., Vermeersen, L., & King, M., 2011. A benchmark study for glacial isostatic adjustment codes, *Geophysical Journal International*, **185**(1), 106–132.

Steffen, H., Kaufmann, G., & Wu, P., 2006. Three-dimensional finite-element modeling of the glacial isostatic adjustment in Fennoscandia, *Earth and Planetary Science Letters*, **250**(1-2), 358–375.

Tanaka, Y., Klemann, V., Martinec, Z., & Riva, R., 2011. Spectral-finite element approach to viscoelastic relaxation in a spherical compressible Earth: application to GIA modelling, *Geophysical Journal International*, **184**(1), 220–234.

Turpeinen, H., Hampel, A., Karow, T., & Maniatis, G., 2008. Effect of ice sheet growth and melting on the slip evolution of thrust faults, *Earth and Planetary Science Letters*, **269**(1-2), 230–241.

van der Wal, W., Whitehouse, P. L., & Schrama, E. J., 2015. Effect of GIA models with 3D composite mantle viscosity on GRACE mass balance estimates for Antarctica, *Earth and Planetary Science Letters*, **414**, 134–143.

Vardić, K., Clarke, P. J., & Whitehouse, P. L., 2022. A GNSS velocity field for crustal deformation studies: The influence of glacial isostatic adjustment on plate motion models, *Geophysical Journal International*.

Vermeersen, L. & Mitrovica, J., 2000. Gravitational stability of spherical self-gravitating relaxation models, *Geophysical Journal International*, **142**(2), 351–360.

Vermeersen, L. & Sabadini, R., 1997. A new class of stratified viscoelastic models by analytical techniques, *Geophysical Journal International*, **129**(3), 531–570.

Wolf, D. et al., 1985. The normal modes of a uniform, compressible Maxwell half-space, *Journal of Geophysics*, **56**(1), 100–105.

Wong, M. C. & Wu, P., 2019. Using commercial finite-element packages for the study of Glacial Isostatic Adjustment on a compressible self-gravitating spherical earth–1: harmonic loads, *Geophysical Journal International*, **217**(3), 1798–1820.

Wu, P., 1992. Viscoelastic versus viscous deformation and the advection of pre-stress, *Geophysical journal international*, **108**(1), 136–142.

Wu, P., 2004. Using commercial finite element packages for the study of earth deformations, sea levels and the state of stress, *Geophysical Journal International*, **158**(2), 401–408.

Wu, P. & Johnston, P., 1998. Validity of using flat-earth finite element models in the study of postglacial rebound, *Dynamics of the ice age earth: A modern perspective*, pp. 191–202.

Wu, P. & Peltier, W., 1982. Viscous gravitational relaxation, *Geophysical Journal International*, **70**(2), 435–485.

Zhong, S., Paulson, A., & Wahr, J., 2003. Three-dimensional finite-element modelling of Earth's viscoelastic deformation: effects of lateral variations in lithospheric thickness, *Geophysical Journal International*, **155**(2), 679–695.

Zwinger, T., Nield, G. A., Ruokolainen, J., & King, M. A., 2020. A new open-source viscoelastic solid earth deformation module implemented in Elmer (v8. 4), *Geoscientific Model Development*, **13**(3), 1155–1164.

submitted to *Geophys. J. Int.*

Supplementary Material for: Simulating horizontal crustal motions of glacial isostatic adjustment using compressible cartesian models

J. M. Reusen,[1] R. Steffen,[2] H. Steffen,[2] B. C. Root,[1] W. van der Wal[1]

[1] *Faculty of Aerospace Engineering, Delft University of Technology, Delft, The Netherlands*

[2] *Lantmäteriet, Gävle, Sweden*

Last compiled: 25 April 2023

CONTENTS

1 Solving the equations in Abaqus
2 Sensitivity to the spherical harmonic truncation limit
3 Spada et al. (2011) benchmark
3.1 Models used for the benchmark
3.2 Results
4 Sensitivity to the Earth model
5 Sensitivity to the resolution of the FEM model
6 Volumetric strain after 10ka of loading in box-NG

1 SOLVING THE EQUATIONS IN ABAQUS

The governing equations are solved using a different solution method for the NG method. To be able to explain the differences with the EF method, we review how the finite element equations are solved within Abaqus. Abaqus solves for the following equation of motion (Hibbitt et al. 2016):

$$\nabla \cdot \boldsymbol{\tau} + \mathbf{f} = 0, \tag{S.1}$$

where $\mathbf{f}$ are the body forces. The equation of motion is solved using the weak formulation which replaces the equations for each of the three directions by a single equation. In order to generate the weak formulation, we multiply equation S.1 by a test function, here considered to be the 'virtual' velocity field $\delta\mathbf{v}$, which is an arbitrary field of sufficient continuity, and integrate over the domain. After some algebra we obtain:

$$\int_S \mathbf{t} \cdot \delta\mathbf{v} + \int_V \mathbf{f} \cdot \delta\mathbf{v} dV = \int_V \boldsymbol{\tau} : \boldsymbol{\delta D} dV. \tag{S.2}$$

Here, $\mathbf{t}$ is the surface traction per unit area at any point on the surface S, defined as $\mathbf{t} = \mathbf{n} \cdot \boldsymbol{\tau}$. Furthermore, $\boldsymbol{\delta D} = \mathrm{sym}\{\nabla\delta\mathbf{v}\}$, the symmetric part of the virtual velocity gradient. $\boldsymbol{\delta D}$ is also known as the virtual strain rate or the virtual rate of deformation. The colon ':' is the double dot product for tensors, where $\boldsymbol{A} : \boldsymbol{B} = A_{ij}B_{ij}$. We can replace the Cauchy stress tensor $\boldsymbol{\tau}$ and the virtual strain rate $\boldsymbol{\delta D}$ in equation S.2 by any conjugate pairing of stress and strain, and choose a stress and strain that are defined relative to a reference volume V_0 (Hibbitt et al. 2016). We arrive at the following equation:

$$\int_S \mathbf{t} \cdot \delta\mathbf{v} + \int_V \mathbf{f} \cdot \delta\mathbf{v} dV = \int_{V_0} \boldsymbol{\tau}^c : \boldsymbol{\delta\epsilon} dV_0. \tag{S.3}$$

Here, $\boldsymbol{\delta\epsilon}$ is the virtual strain rate associated with $\delta\mathbf{v}$, and $\boldsymbol{\tau}^c$ is the conjugate stress. The specific strain rate that we use for $\boldsymbol{\delta\epsilon}$ depends on the individual elements. Equation S.3 is then discretized by introducing shape functions $\mathbf{N}$ for the deformations $\mathbf{u}$. For simplicity, we show the case for only two dimensions, so $\mathbf{u}$ contains $u(x,y)$ and $v(x,y)$ for the nodal displacement in x and in y, respectively. We get for eight nodal elements:

$$u(x,y) \approx \sum_{N=1}^{8} N_N(x,y)\widetilde{u}^N, \tag{S.4}$$

$$v(x,y) \approx \sum_{N=1}^{8} N_N(x,y)\widetilde{v}^N. \tag{S.5}$$

Here u_i and v_i are the displacement at the nodes. In matrix form:

$$\mathbf{u} = \begin{Bmatrix} u(x,y) \\ v(x,y) \end{Bmatrix} = \left[\begin{array}{cc:cc:cc} N_1 & 0 & N_2 & 0 & \cdots & \cdots \\ 0 & N_1 & 0 & N_2 & \cdots & \cdots \end{array}\right] \left\{\begin{array}{c} u_1 \\ v_1 \\ \hdashline u_2 \\ v_2 \\ \hdashline \vdots \\ \vdots \end{array}\right\}. \tag{S.6}$$

Similarly, we obtain for the virtual velocity field $\delta\mathbf{v}$:

$$\delta\mathbf{v} = \mathbf{N}_N \widetilde{\delta v}^N. \tag{S.7}$$

Here $\mathbf{N}_N$ are the shape functions of row N, and $\widetilde{\delta v}^N$ is the Nth element of the virtual velocity field at the nodes. $\boldsymbol{\delta\epsilon}$ is equal to

$$\boldsymbol{\delta\epsilon} = \boldsymbol{\beta}_N \widetilde{\delta v}^N, \tag{S.8}$$

where $\boldsymbol{\beta}_N$ is the strain-displacement matrix. It is the derivative of $\mathbf{N}_N$ with respect to the position:

$$\boldsymbol{\beta}_N = \begin{bmatrix} \frac{\partial N_N}{\partial x} & 0 \\ 0 & \frac{\partial N_N}{\partial y} \\ \frac{\partial N_N}{\partial y} & \frac{\partial N_N}{\partial x} \end{bmatrix}. \tag{S.9}$$

We get from equation S.3 after cancelling the commen factor $\widetilde{\delta v}^N$:

$$\int_{V_0} \boldsymbol{\beta}_N : \boldsymbol{\tau}^c dV_0 - \int_S \mathbf{N}_N^T \cdot \mathbf{t} dS - \int_V \mathbf{N}_N^T \cdot \mathbf{f} dV = 0. \tag{S.10}$$

Here the superscript T refers to the transpose of $\mathbf{N}_N$. We can work this out further, using the definition for $\boldsymbol{\tau}^c$:

$$\boldsymbol{\tau}^c = \mathbf{H} : \boldsymbol{\beta}_M \widetilde{u}^M. \tag{S.11}$$

Here, $\mathbf{H}$ is a fourth order tensor containing material properties which is the proportionality constant in the stress-strain relation, and the summation is over node M. The equation of motion is now as follows:

$$\widetilde{u}^M \int_{V_0} \boldsymbol{\beta}_N : \mathbf{H} : \boldsymbol{\beta}_M dV_0 = \int_S \mathbf{N}_N^T \cdot \mathbf{t} dS + \int_V \mathbf{N}_N^T \cdot \mathbf{f} dV, \tag{S.12}$$

which is of the form $K_{NM} u_M = f_N$ solved by the FE software Abaqus, with K_{NM} the stiffness matrix:

$$K_{NM} = \int_{V_0} \boldsymbol{\beta}_N : \mathbf{H} : \boldsymbol{\beta}_M dV_0. \tag{S.13}$$

This stiffness matrix is used by the Elastic Foundations method.

2 SENSITIVITY TO THE SPHERICAL HARMONIC TRUNCATION LIMIT

Normal mode model SM-I uses spherical harmonic (SH) degrees in the horizontal direction. In the main paper, the maximum amount of SH degrees is 256. Here, we test how much more accurate a cut-off degree of 512 is for our results in the horizontal. Increasing the maximum SH degree from 256 to 512 only improves our results by 0.01 m at most, with this maximum difference situated around the ice edge (Figure S1). The maximum horizontal displacement is -11 m, and thus this difference is deemed insignificant for the results of this study.

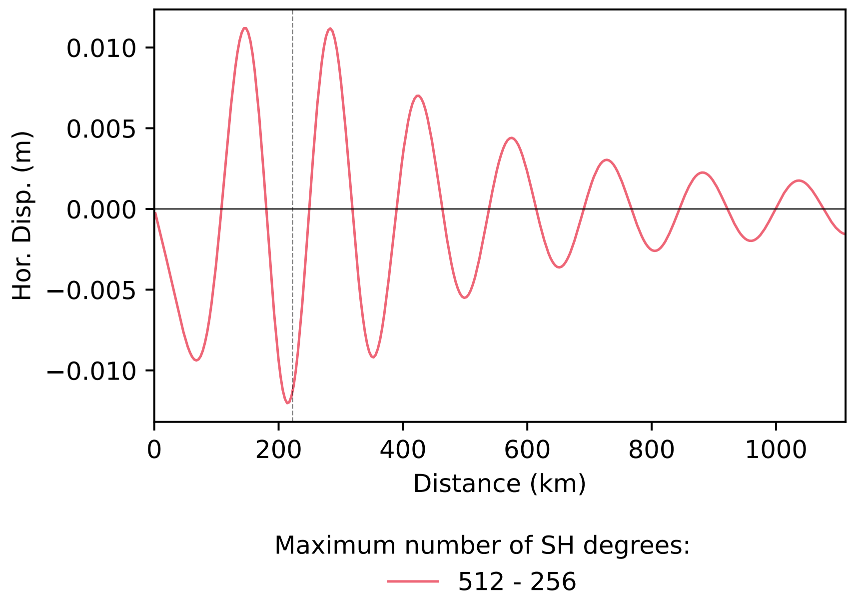

Figure S1. Difference in modelled horizontal displacement after 10ka of loading with a disc load 222 km in radius.

3 SPADA ET AL. (2011) BENCHMARK

Our first benchmark was with results using the Earth model described in Spada et al. (2011). For this benchmark, we also used AFCAL, a spherical FE code that has been benchmarked in Martinec et al. (2018), and FastLove-HiDeg, a normal mode code which is validated in Spada et al. (2011). These two models are described in more detail below. The simulations for this benchmark consists of 4 Earth layers (5 boundaries), each divided into 12 FE elements in the vertical direction for the box models. Using 16 cores, a computation time is achieved of 16-18 hours for the incompressible runs with the box models. We compare the vertical displacement and subtract the value in the far field from the FE model results, as both FE box models in this study differ by about 1.5 meters in the far field. We perform this correction in the same way as Hampel et al. (2019), and the output of the box models is hence shown with respect to the upper right corner of the model.

3.1 Models used for the benchmark

3.1.1 AFCAL

The AFCAL model is a spherical axisymmetric FE model using elastic foundations (Wu & van der Wal 2003; van der Wal et al. 2010), and is used in benchmark A of Martinec et al. (2018). The viscous deformation is computed by ABAQUS, and the self-gravity is calculated by solving for the gravitational potential using the SH method in the Laplace domain. It contains a tangential resolution of 0.0625 degrees and a radial resolution of at least 4 elements per layer, double than what is used in Martinec et al. (2018), as the deformation due to the 2 degree load is found to be sensitive both to horizontal and the vertical resolution. Poisson's ratio is set to 0.495, in order to prevent volumetric locking. The change in gravitational potential is applied as a force at the boundaries for the next iteration (as in Wu 2004). Four iterations are used, as was also done in Martinec et al. (2018).

3.1.2 FastLove-HiDeg

The normal mode code FastLove-HiDeg uses the multilayer matrix propagation method (Vermeersen & Sabadini 1997), and has been benchmarked in Spada et al. (2011). This model will be used as a reference for all the other incompressible models. 512 SH degrees are used for the computation. The horizontal resolution of the model is 0.03125 degrees, which is mostly an oversampling, since the resolution is effectively determined by the amount of SH degrees available in the model.

3.2 Results

The NMM codes SM-I and FastLove-HiDeg match excellently, and diferences are everywhere below 1 (Figure S2). The residual in the vertical displacement between the spherical FE model peak at the edge of the ice sheet with values just below 3%.

The vertical displacements for the box models are expected to differ a little from the spherical models, but still match well, with differences below 3% under the ice sheet for four out of 5 ice sheet simulations. This is in agreement with Amelung & Wolf (1994) and Wu & Johnston (1998),

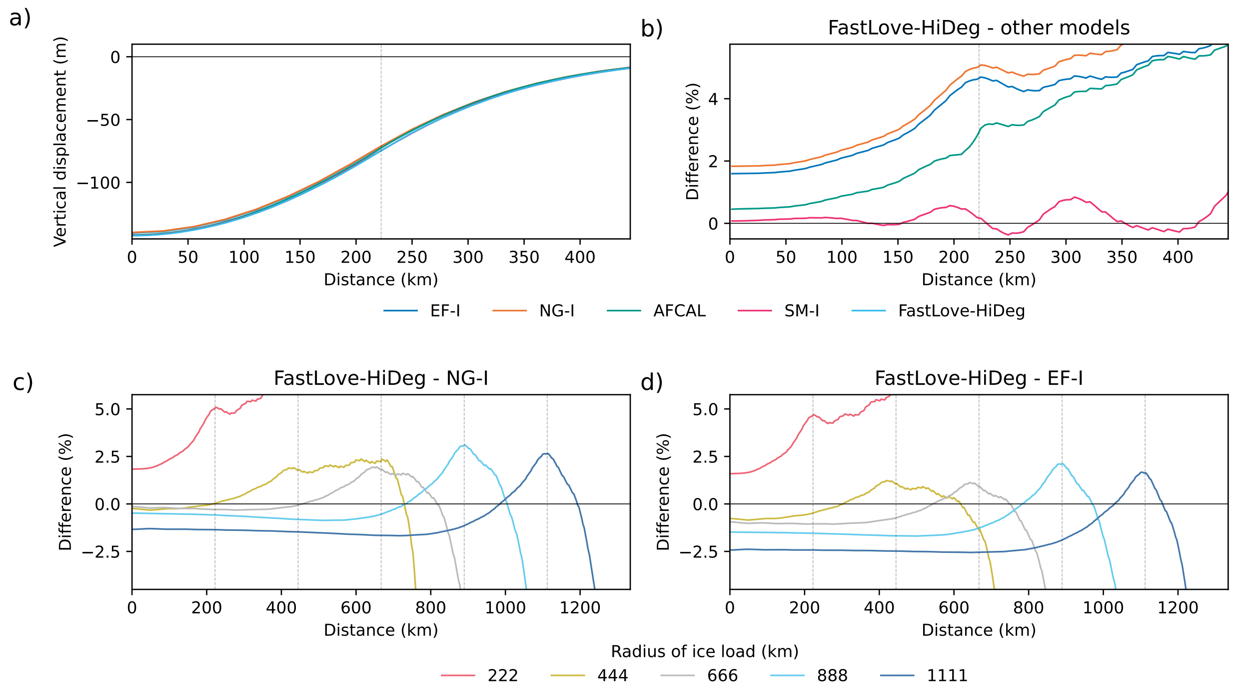

Figure S2. Vertical displacement for the incompressible models for a disc 2 degrees in extent (a), as well as the difference in vertical displacement rate with FastLove-HiDeg (b). The bottom subplots show the difference in vertical displacement between FastLove-HiDeg and NG-I (c) and box-EF (d), respectively, for discs with 5 different radii. The ice edges are denoted by the dashed vertical lines.

who found that box models provide an acceptable level of accuracy in the vertical for ice sheets the size of the Fennoscandian ice sheet.

4 SENSITIVITY TO THE EARTH MODEL

The compressible spherical model SM needs many layers to be stable. Because of this, it employs PREM, with a resolution of 1 km in the vertical. This inherently results in differences compared to models that employ constant layer values, like Abaqus. The constant layer values can be approximated in SM-I, and compared with the incompressible PREM Earth model. This way, we can obtain more information on the sensitivity to the Earth model. Using the 10 ka loading scenario, differences in the horizontal displacement are fluctuating between 5 and 7% for the 222 km and 1,111 km radius ice sheet, with a peak of 12% around the ice edge for the simulation with the larger ice sheet (Figure S3). Using the unloading scenario for the horizontal displacement rates,

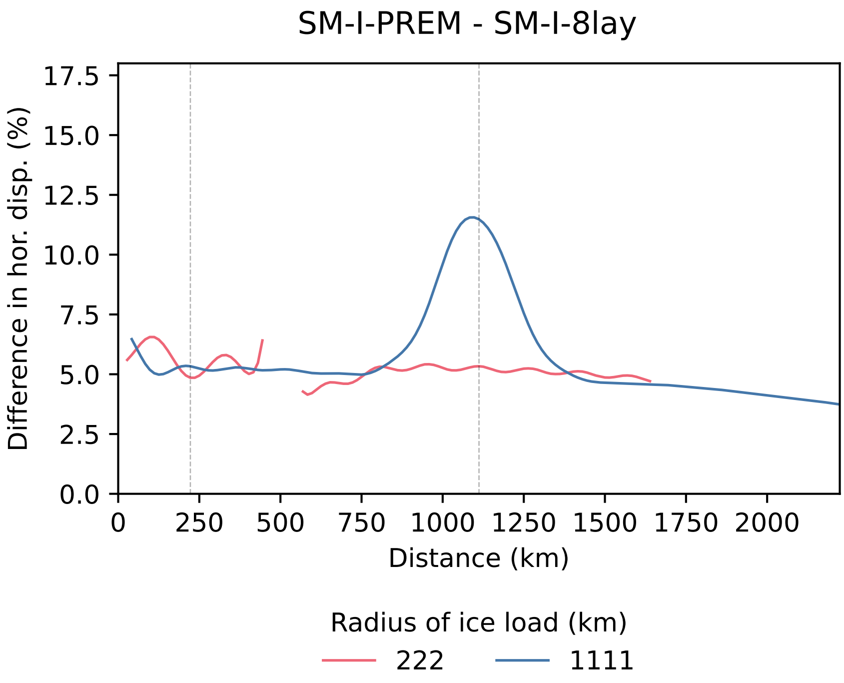

Figure S3. Difference in horizontal displacement due to the Earth model approximation for the incompressible ICEAGE model, using 10 ka of loading. When the absolute value of the original signal is below 1.5m, the values are masked.

106 differences are found to be up to 10% close to the load center, decreasing to 5% just outside of the
107 load (Figure S4).

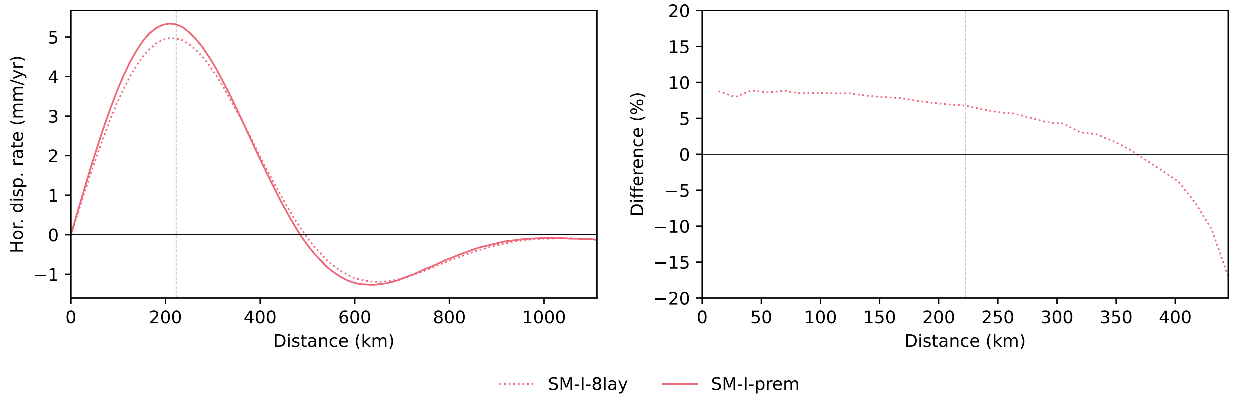

Figure S4. Using the unloading scenario, (a) simulated horizontal displacement rate, and (b) differences in horizontal displacement rate due to the Earth model approximation for the incompressible ICEAGE model.

5 SENSITIVITY TO THE RESOLUTION OF THE FEM MODEL

We test the effect of the vertical and horizontal resolution in our finite element models NG-I and EF-I. The vertical resolution shows little sensitivity to an increase in the vertical amount of seeds in a layer (Figure S5). There appears to be a little more sensitivity in NG-I as compared to EF-I, especially in the far field. We opt for 4 vertical seeds per Earth model layer in our box models, as 5 vertical seeds is deemed unnecessary, and models with a resolution of 4 vertical seeds per Earth layer can still be run within reasonable computation time ($\sim$ 4 hours).

The horizontal resolution shows a higher sensitivity to the modelled horizontal displacement, and a clear visual improvement can be seen in Figure S6 when increasing the horizontal resolution in the high resolution region from 222 km to 27 km. NG-I and EF-I exhibit an almost identical sensitivity to the horizontal resolution. We decided to employ the finest horizontal resolution tested (27 km) in all other simulations of this paper.

6 VOLUMETRIC STRAIN AFTER 10KA OF LOADING IN BOX-NG

Compressibility is related to the dilatation of the elements, and the corresponding increase or decrease in density, assuming that the mass of each element is conserved. Therefore, we plot the volumetric strain, $\frac{\Delta V}{V}$, which is calculated as the sum of the three diagonal strain components:

$$\frac{\Delta V}{V} = \epsilon_{11} + \epsilon_{22} + \epsilon_{33} \tag{S.14}$$

There is compression under the ice load and expansion just outside of the ice load. The minimum value of -15 for the volumetric strain implies a density increase of roughly 0.45 kg/m^3 (average crustal density of 3000 kg/m^3 multiplied with -15 $\times 10^{-5}$). This is reasonable, as the strain scales as $|$u$|$/wavelength (Pollitz 1997). In the case of 10 ka loading with a 1111 km radius load, the deformation is dominant in the vertical and about 200 m. The wavelength of the load is twice the radius and therefore equal to 2222 km. $|$u$|$/wavelength then roughly equals 200 m / 2222 km which is equal to just under 1×10^{-4}, similar in magnitude to what is found here for the volumetric strain.

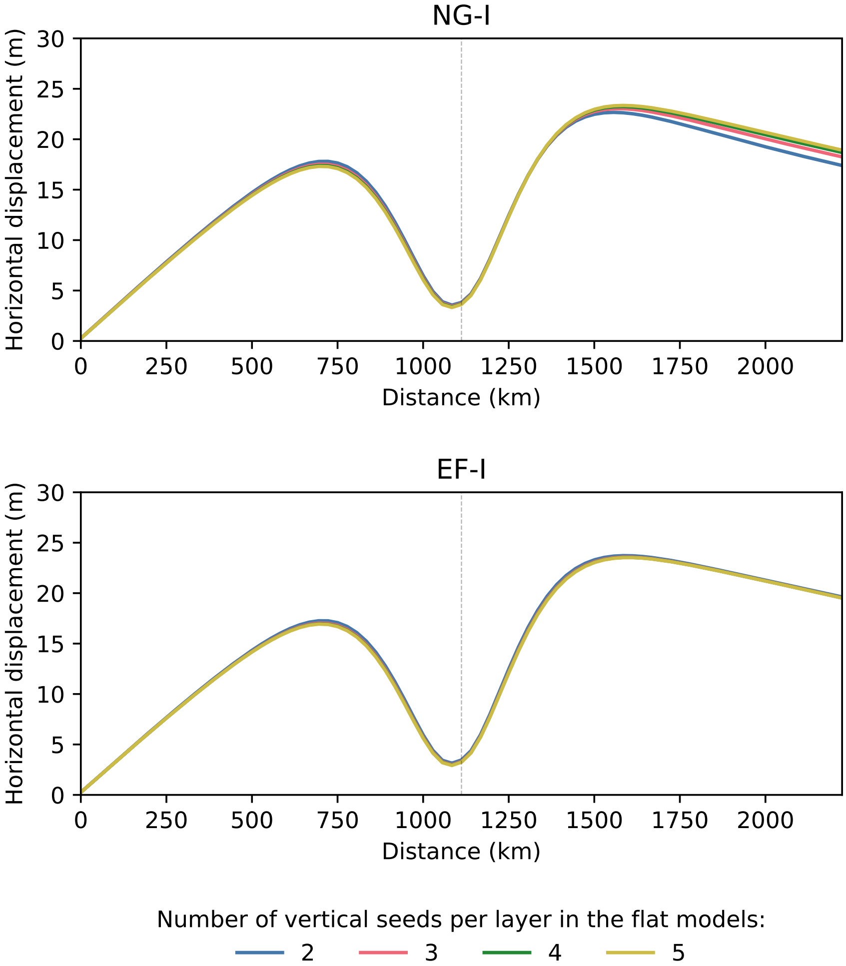

Figure S5. Difference in horizontal displacement after 10ka of loading for NG-I (a) and EF-I (b) due to changing the amount of elements per layer, for the 1111 km radius disc load.

The Lithosphere-Asthenosphere Boundary (LAB) exhibits a clear boundary for the volumetric strain of the elements, as just above this boundary values are positive, and below we find negative values again. This implies that material in the uppermost layer of the mantle compresses more than the lowest elemental layer in the crust. The most negative strain is found just below the surface, as anticipated.

REFERENCES

Amelung, F. & Wolf, D., 1994. Viscoelastic perturbations of the earth: significance of the incremental gravitational force in models of glacial isostasy, *Geophysical Journal International*, **117**(3), 864–879.

Hampel, A., Lüke, J., Krause, T., & Hetzel, R., 2019. Finite-element modelling of glacial isostatic ad-

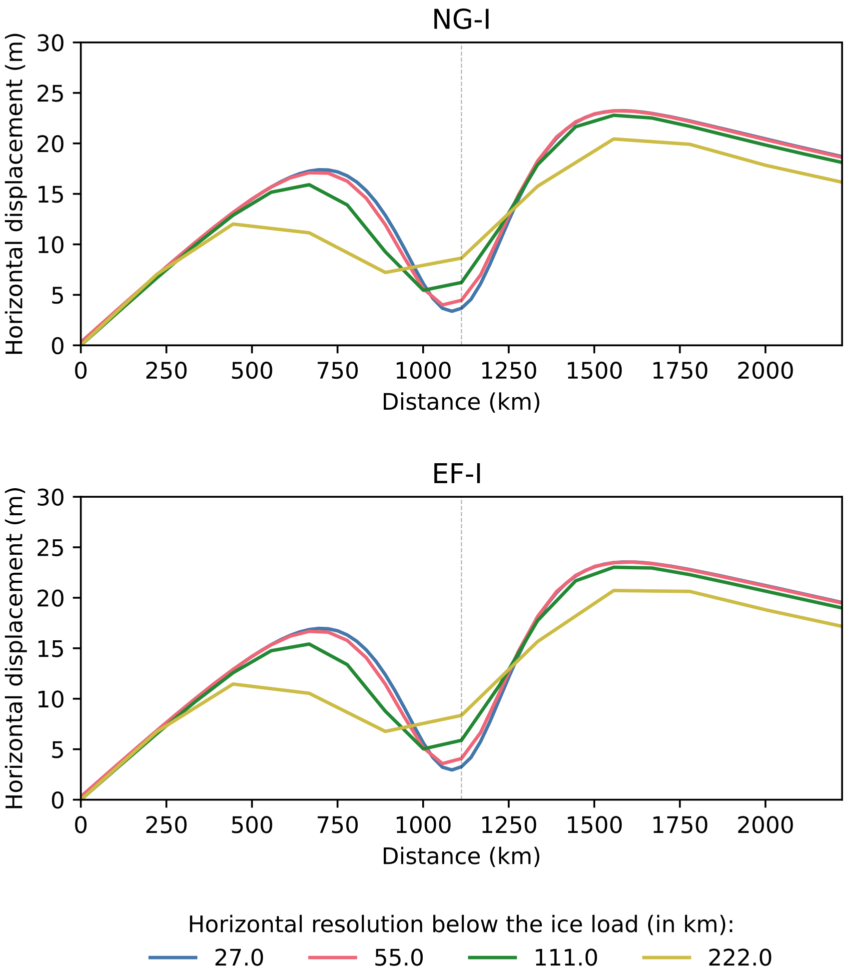

Figure S6. Difference in horizontal displacement after 10ka of loading for NG-I (a) and EF-I (b) due to changing the horizontal resolution below the load, for the 1111 km radius disc load.

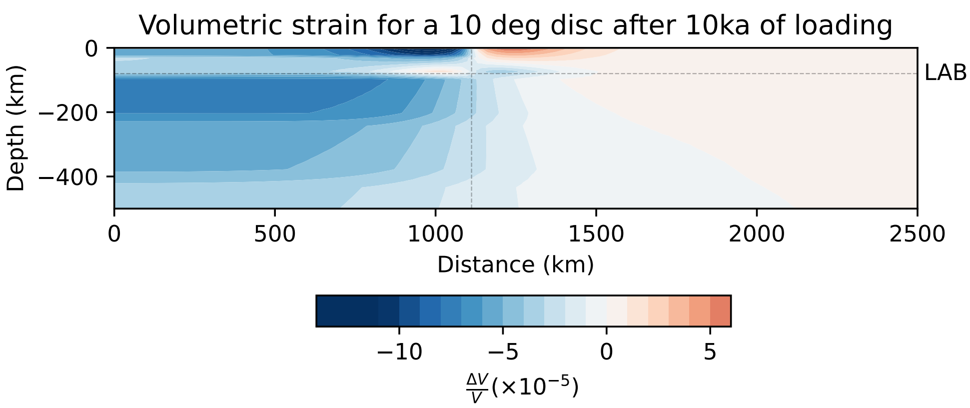

Figure S7. Volumetric strain after 10ka of loading with a 10 deg disc in box-NG. Positive values denote compression, and negative values dilatation. The Lithosphere-Asthenosphere Boundary (LAB) is denoted by the horizontal dashed line.

justment (GIA): Use of elastic foundations at material boundaries versus the geometrically non-linear formulation, *Computers & geosciences*, **122**, 1–14.

Hibbitt, D., Karlsson, B., & Sorensen, P., 2016. Getting started with ABAQUS, version (6.14), *Hibbit, Karlsson & Sorensen, Inc*.

Martinec, Z., Klemann, V., van der Wal, W., Riva, R., Spada, G., Sun, Y., Melini, D., Kachuck, S., Barletta, V., Simon, K., et al., 2018. A benchmark study of numerical implementations of the sea level equation in GIA modelling, *Geophysical Journal International*, **215**(1), 389–414.

Pollitz, F. F., 1997. Gravitational viscoelastic postseismic relaxation on a layered spherical Earth, *Journal of Geophysical Research: Solid Earth*, **102**(B8), 17921–17941.

Spada, G., Barletta, V. R., Klemann, V., Riva, R., Martinec, Z., Gasperini, P., Lund, B., Wolf, D., Vermeersen, L., & King, M., 2011. A benchmark study for glacial isostatic adjustment codes, *Geophysical Journal International*, **185**(1), 106–132.

van der Wal, W., Wu, P., Wang, H., & Sideris, M. G., 2010. Sea levels and uplift rate from composite rheology in glacial isostatic adjustment modeling, *Journal of Geodynamics*, **50**(1), 38–48.

Vermeersen, L. & Sabadini, R., 1997. A new class of stratified viscoelastic models by analytical techniques, *Geophysical Journal International*, **129**(3), 531–570.

Wu, P., 2004. Using commercial finite element packages for the study of earth deformations, sea levels and the state of stress, *Geophysical Journal International*, **158**(2), 401–408.

Wu, P. & Johnston, P., 1998. Validity of using flat-earth finite element models in the study of postglacial rebound, *Dynamics of the ice age earth: A modern perspective*, pp. 191–202.

Wu, P. & van der Wal, W., 2003. Postglacial sealevels on a spherical, self-gravitating viscoelastic earth: effects of lateral viscosity variations in the upper mantle on the inference of viscosity contrasts in the lower mantle, *Earth and Planetary Science Letters*, **211**(1-2), 57–68.